

1 Lung Tumor Microphysiological System with 3D Endothelium to Evaluate Modulators of T-Cell
2 Infiltration

3 Katrina M. Wisdom^{1*}, Johnny Suijker⁷, Lenie van den Broek⁷, BanuPriya Sridharan¹, Taraka Sai
4 Pavan Grandhi¹, Aaron Cheng², Mahdi Lamb³, Steven A. Titus², Andrew Gehman⁶, Derek
5 Poore⁴, Niyant Shah⁴, Shih-Hsun Cheng¹, Edward Kim⁴, Sue Griffin⁵, and Jason Ekert¹

6 ¹*In Vitro In Vivo Translation, Research, Pharmaceutical R&D, GSK, 1250 S. Collegeville Rd, Collegeville, PA, USA*

7 ²*Genomic Sciences, Research, Pharmaceutical R&D, GSK, 1250 S. Collegeville Rd, Collegeville, PA USA*

8 ³*Genomic Sciences, Research, Pharmaceutical R&D, GSK, Gunnels Wood Rd, Stevenage SG1 2NY, UK*

9 ⁴*Immuno-Oncology, Research, Pharmaceutical R&D, GSK, 1250 S. Collegeville Rd, Collegeville, PA USA*

10 ⁵*Immuno-Oncology, Research, Pharmaceutical R&D, GSK, Gunnels Wood Rd, Stevenage SG1 2NY, UK*

11 ⁶*Development Biostatistics, Development, Pharmaceutical R&D, GSK, 1250 S. Collegeville Rd, Collegeville, PA USA*

12 ⁷*Mimetas B.V., Biopartner Building 5, De Limes 7, 2342 DH Oegstgeest, The Netherlands*

13

14 *Corresponding author contact information: katrina.m.wisdom@gsk.com

15 Key words: Microphysiological system, Tumor Microenvironment, T-Cells, Chemotaxis,
16 Angiogenesis

17

18 **Abstract**

19 Lung cancer is a leading cause of death worldwide, with only a fraction of patients responding to
20 immunotherapy. The correlation between increased T-cell infiltration and positive patient
21 outcomes has motivated the search for therapeutics promoting T-cell infiltration. While transwell
22 and spheroid platforms have been employed, these models lack flow and endothelial barriers,
23 and cannot faithfully model T-cell adhesion, extravasation and migration through 3D tissue.
24 Presented here is a 3D chemotaxis assay, in a lung tumor on chip model with 3D endothelium
25 (LToC-Endo), to address this need. The described assay consists of a vascular tubule cultured
26 under rocking flow, through which T-cells are added; a collagenous stromal barrier, through which
27 T-cells infiltrate; and a chemoattractant/tumor compartment. Here, activated T-cells extravasate
28 and infiltrate in response to gradients of rhCXCL11 and rhCXCL12. Adopting a T-cell activation
29 protocol with a rest period enables proliferative burst prior to introducing T-cells into chips,
30 increases T-cell expression of CXCR3 and CXCR4 receptors, and enhances assay sensitivity. In
31 addition, incorporating this rest recovers endothelial activation in response to rhCXCL12. As a
32 final control, we show that blocking ICAM-1 interferes with T-cell adhesion and chemotaxis. This
33 microphysiological system, which mimics *in vivo* stromal and vascular barriers, can be used to
34 evaluate potentiation of immune chemotaxis into tumors while probing for vascular responses to
35 potential therapeutics. Finally, we propose a translational strategy by which this assay could be
36 linked to preclinical and clinical models to support human dose prediction, personalized medicine,
37 and the reduction, refinement, and replacement of animal models.

38

39

40

41

42

43 Introduction

44 Although immunotherapy has shown great promise, immune cell infiltration into the tumor
45 microenvironment of many indications and/or sub-indications remains challenging, leading to
46 mixed clinical outcomes[1]–[3]. Patients with “inflamed” tumors, in which immune cells are
47 inhibited but in close contact with tumor cells, typically respond better to cancer immunotherapy
48 and experience better prognoses[4], [5]. By contrast, patients tend to experience poorer outcomes
49 if their tumors are “immune excluded”, in which cytotoxic T-cells have accumulated in the tumor
50 stroma but are not able to reach the tumor cells, or “immune desert”, in which cytotoxic T-cells
51 are absent from both the tumor nest and stroma[4], [5]. Given that a high presence of cytotoxic T-
52 cells in tumors is correlated with improved patient survival, there is a strong need to enhance T-
53 cell chemotaxis into tumors and enhance the effectiveness of immunotherapies[1]–[3], [5], [6].
54 Despite the clear rationale to address this aspect of the cancer-immunity cycle, there are limited
55 potential therapeutics available to address it [6].

56 While preclinical *in vivo* models have ushered in pivotal treatments in cancer immunotherapy
57 (e.g., anti-CTLA-4 and anti-PD-(L)1), the limited translatability of preclinical models is a key
58 challenge for the development of many immunotherapies[4]. Genetically engineered mouse
59 models have evolved as the closest representation of human cancers, but differences in species-
60 specific immunology and disease progression between mouse and human tumors hamper their
61 clinical translatability[4], [7]. Furthermore, increasing global attention on ethical issues with animal
62 research has bolstered support for initiatives to refine, reduce, and replace animal models[8].

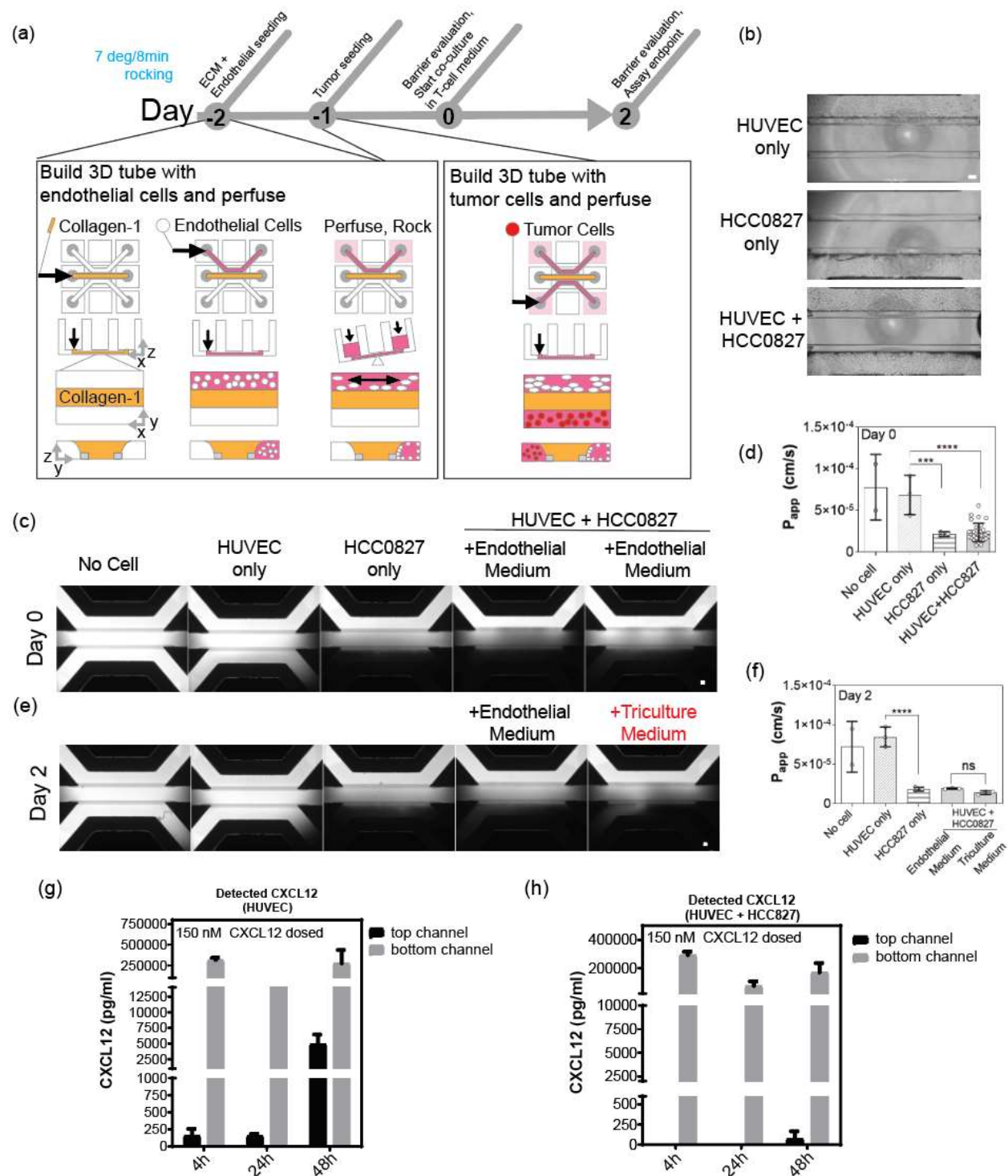
63 *In vitro*, Transwell migration systems have been employed to investigate modulators of cell
64 migration and chemotaxis. However, the effects of chemotactic triggers on migrating cells over
65 long time windows remains challenging in these platforms due to gravity and gradient
66 instability[9]–[11]. Furthermore, these platforms are unable to recapitulate some aspects of the
67 tumor microenvironment. Transwell membranes with rigid pores are unable to model dynamic cell
68 extravasation through living, responsive vasculature or 3D cell migration through viscoelastic and
69 mechanically plastic pores of extracellular matrix[12]. Furthermore, as chemotaxis takes place
70 along the z-axis in these assays, large confocal z-stacks, which may be time and data intensive
71 to acquire and process, may be necessary to obtain single cell-resolution migration information.
72 Alternatively, 3D spheroids are valuable for modeling T-cell infiltration into tumor nests [13]–[15].
73 However, optical clearing is necessary in order to image inside spheroids beyond 200 μm , which
74 can only be done as an endpoint analysis. Furthermore, spheroid assays do not always model
75 the extracellular matrix of solid tumors, even though dense stromal matrix is known to physically
76 prevent infiltration in human lung tumors[16]. Additionally, growing evidence suggests that T-cells
77 exhibit distinct kinds of motility dependent on both their activation state and features of their
78 microenvironment[17]. For these reasons, infiltration studies with spheroids alone may not be
79 sufficient to model the stromal constituents contributing to antitumor immunity in “immune
80 excluded” and “immune desert” tumors.

81 While transwell and spheroid models can be informative and high throughput, they also lack a
82 living endothelial barrier and vascular flow. For this reason, these platforms cannot be used to
83 model extravasation, an early stage of T-cell chemotaxis into tumors. There is a need for an
84 integrated complex *in vitro* model to investigate multiple stages of T-cell chemotaxis, including T-
85 cell adhesion, extravasation, and infiltration through a 3D stromal barrier, to evaluate therapeutics
86 that could enable T-cells to overcome these barriers and directly contact tumor cells, thereby
87 enhancing the effectiveness of immunotherapies. For maximum utility in drug discovery and

88 development, it should be phenotypic-screening amenable, offering single cell resolution readouts
89 without being time and data intensive to image or analyze.

90 Recent developments in organ-on-chip technologies have been encouraging, but many of these
91 early models are low throughput, made of polydimethylsiloxane (PDMS) (a hydrophobic material
92 known to nonspecifically adsorb proteins), and contain artificial membranes[18]. The MIMETAS
93 3-lane Organoplate® is a platform containing 40 chips per plate, no PDMS, and phase guide
94 technology, which enables membrane-free material separation. Recently, this platform was used
95 to investigate monocyte-to-endothelium adhesion, neutrophilic infiltration, and 3D T-Cell
96 chemotaxis in a melanoma model[18]. Building upon these models, we established a lung tumor
97 on chip model with 3D endothelium (“LToC-Endo”) to investigate immune cell chemotaxis in
98 response to chemokines and antibody treatments. Here we show that activated T-cells in the
99 LToC-Endo model adhere, extravasate, and infiltrate in response to gradients of rhCXCL11 and
100 rhCXCL12 (referred to throughout the manuscript as “CXCL11” and “CXCL12”), and that
101 simultaneously, the living endothelial barrier responds to CXCL12 by sprouting. Using this assay,
102 we show functional differences between T-cells activated using different approaches, and can
103 inhibit infiltration by perturbing canonical endothelial receptor-T-cell receptor interactions.

104



105

106

107

108

109

110

111

112

113

Figure 1: T-cell chemotaxis assay development, medium evaluation, and barrier analysis in the LToC-Endo model. (a) Experimental setup and timeline of platform seeding with Collagen-1, endothelial cells, and tumor cells. (b) Representative images of the platform seeded in monoculture and coculture configurations, with endothelial medium and triculture assay medium, on day 0. The transition from endothelial medium to triculture assay medium occurs on day 0 to mimic T-cell seeding at that time point. Refer to Fig S1 for information on the different assay

114 media formulations considered. (c) and (e), Barrier integrity assay fluorescence images, where
115 white shows FITC dextran presence. (d) and (f), permeability coefficient measurements for
116 different configurations of the assay, for day 0 and day 2, respectively. Data show measurements
117 per chip for $n=2$ or $n>2$ chips per condition for those used for statistical testing, bars indicate
118 means, and error bars indicate standard deviations. Data was square root transformed prior to
119 statistical testing to account for unequal variances. Outcomes are indicated for statistical tests
120 comparing barrier diffusivity among the conditions tested (One-way ANOVA, $***p < 0.001$,
121 $****p < 0.0001$). (g) and (h), ELISA data of CXCL12 concentration in the bottom and top channels
122 48h after 150 nM CXCL12 is first introduced into the bottom channels of the chips. Data show
123 measurements per chip for $n = 2$ chips per condition. The bars represent means and error bars
124 indicate SD, and error bars indicate standard deviations. The scale bars in (b), (c), and (e) are
125 100 μm .

126 **Results and Discussion**

127

128 *Tumor barrier limits chemokine diffusion throughout tumor chips with 3D endothelium*

129

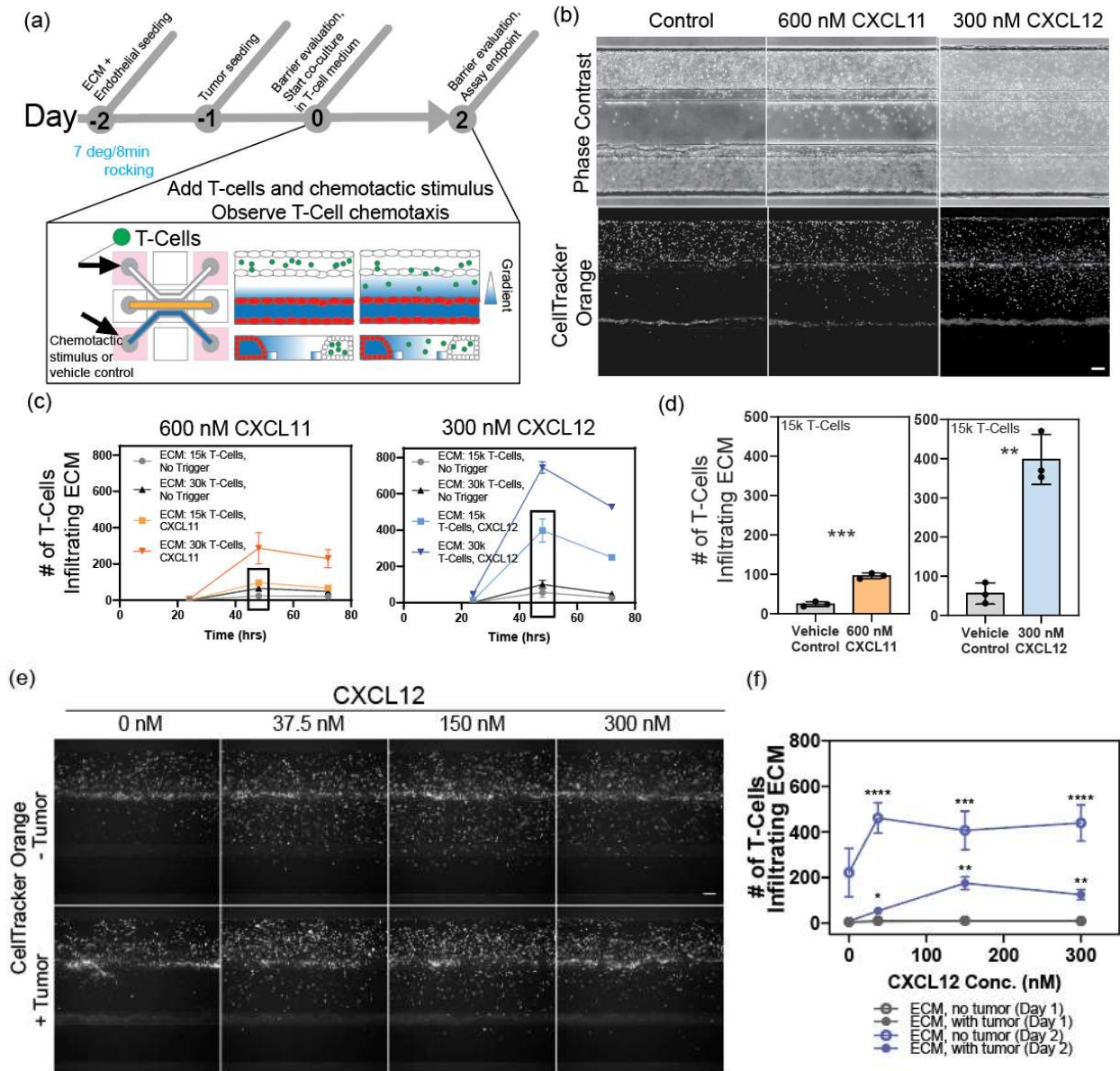
130 We developed a lung tumor on chip model with 3D endothelium (“LToC-Endo”) in the MIMETAS
131 3-lane Organoplate® using three human cell types: pooled donor human umbilical vein
132 endothelial cells (HUVEC), HCC0827 non-small cell lung carcinoma cell line, and primary T-cells.
133 First, we established a collagen-1 extracellular matrix barrier. Then, we seeded endothelial cells
134 in the top channel of the Organoplate® against this barrier on day -2, and cultured the chips under
135 rocking flow (Fig 1a). The following day (day -1), we seeded tumor cells and by day 0, we
136 observed that both the endothelial cells and tumor cells formed tubules in the top and bottom
137 lanes, respectively (Fig 1b).

138

139 To evaluate the diffusivity of both the endothelial and tumor barriers in the LToC-Endo, we
140 performed two different assays. First, using an imaging-based barrier integrity assay, we added
141 20 kDa fluorescent dextran (approximately the size of chemotactic chemokines) on day 0 into the
142 top endothelial channel, and observed dextran flow through the chips over time with fluorescence
143 microscopy (Fig 1c). By comparing permeability coefficients throughout different chip
144 configurations, we noticed that the 3D endothelial tube readily allowed diffusion, and was
145 comparable to no-cell chip controls (Fig 1c-f). The tumor tubule formed a more diffusion-limiting
146 barrier than the endothelial cells, explaining why the combination of barriers is also significantly
147 more diffusion-limiting than the endothelial barrier alone (Fig 1c-f). This finding was corroborated
148 by an ELISA-based permeability assay, in which CXCL12 chemokine was added into the bottom
149 channel, such that it flowed into the tumor tubule or empty channel and then diffused upward
150 through the chip (Fig 1g,h). Media sampling over time revealed that in the no-tumor version of the
151 assay, chemokine was detectable in the top channel as early as 4 hours, and increased markedly
152 by the 48h time point, with a gradient remaining by this time. By contrast, with a tumor tubule, we
153 could not detect any chemokine in the top channel after 48 hours, at which point the chemokine
154 concentration in the top channel was comparable to, or less than, that of the no-tumor assay after
155 only 4 hours. Altogether, these diffusion studies support that this assay models leaky tumor
156 vasculature near a diffusion-limiting NSCLC tumor.

157

158 To make the LToC-Endo amenable to T-cell addition, we explored the impact of an assay medium
159 switch on day 0 and then evaluated the corresponding platform permeability in addition to
160 endothelial cell number and phenotype (Fig 1b,e,and f; Fig S1). We selected AIM V medium,
161 supplemented with 5 ng/mL recombinant human VEGF (165 isoform) and bFGF, based on its
162 ability to promote markers of endothelial tube stability without appreciably changing barrier
163 diffusion properties.



164

165

166

167 **Figure 2: T-cell seeding density, chemokine type and dose, and tumor barrier presence**

168 **regulate T-cell infiltration in the LToC-Endo model.** (a) Experimental setup and timeline with

169 platform seeding of extracellular matrix, endothelial cells, tumor cells, and T-cells. (b)

170 Representative phase contrast and fluorescence images of T-cell infiltration into the collagen

171 barrier of the tumor on chip, in response to chemokines CXCL11, CXCL12, vehicle controls.

172 Images depict data using a T-cell seeding density of 15,000 cells/chip. (c) Number of infiltrated

173 T-cells, by seeding density and over time, in CXCL11 and CXCL12 and respective plate controls,

174 with data points indicating means of n = 3 chips and error bars indicating SD. 48-hour time point

175 data is highlighted in (d), with bars indicating means of n = 3 chips per condition and error bars

176 indicating SD. Results shown for Welch's t-tests to accommodate unequal variances (** p < 0.01,

177 *** p < 0.001). (e) Representative fluorescent images of T-cell infiltration, for chips by dose of

178 CXCL12 chemokine, with and without tumor barriers, at the day 2 time point. (f) Number of

179 infiltrated T-cells by CXCL12 chemokine dose, with and without tumor barriers, at Day 1 and Day

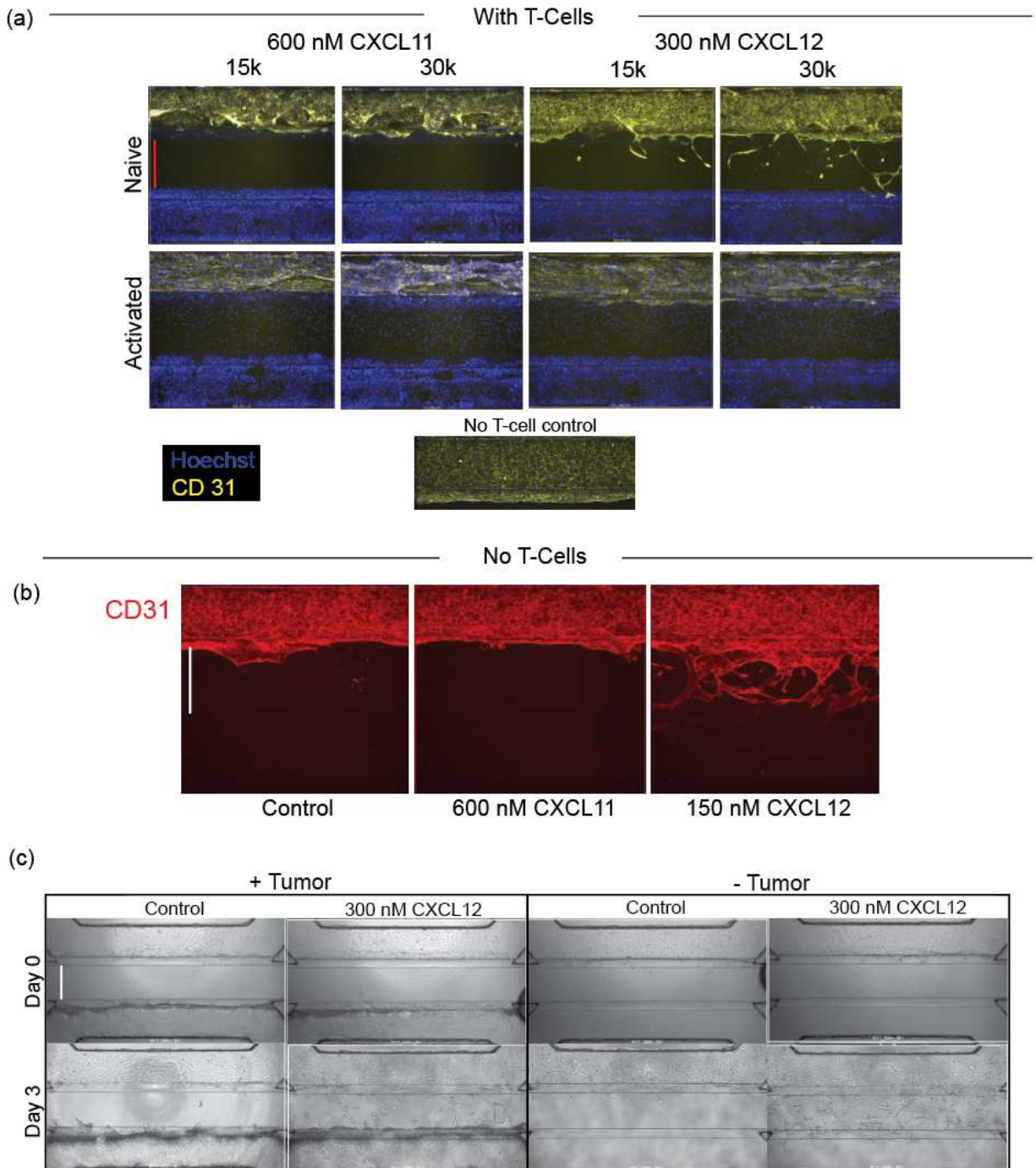
180 2 time points. Day 1 data for tumor and no tumor conditions are overlapping. Markers indicate

181 means of $n \geq 6$ chips per condition, and error bars indicate SEM. Significant differences between
182 CXCL12 dosages and respective vehicle controls are shown (Brown-Forsythe and Welch ANOVA
183 tests, corrected for multiple comparisons, * $p < 0.05$, ** $p < 0.01$, *** $p < 0.001$, **** $p < 0.0001$).
184 Central channel scale bars in (b) and (e) are 100 μm .

185 *Activated, but not naïve, T-cells infiltrate in response to chemokine gradients in the tumor chips*
186 *with 3D endothelium*

187
188 Next, we used the LToC-Endo model to study the effect of activation status, T-Cell seeding
189 density, tumor barrier presence, and chemoattractant type on T-cell chemotaxis. On day 0, we
190 seeded either naïve or activated primary human T-cells into the endothelial channel of the tumor
191 chip, along with recombinant CXCL11 or CXCL12 in the bottom tumor channels (Fig 2a). While
192 naïve T-Cells did not appear to infiltrate into the ECM compartment, activated T-Cells infiltrated
193 the ECM compartment in a seeding density-dependent manner by the day 2 time point after T-
194 cell seeding, in response to both chemokines (Fig 2b-d, Fig. S2). We observed significant
195 differences between chemokine and vehicle control chips (Fig 2c,d). These data are consistent
196 with ELISA data previously shown, illustrating limited chemokine diffusion to the top channel until
197 a 48-hour time point when a tumor barrier is present (Fig 1h).

198
199 We then evaluated the role of chemoattractant dose and tumor presence on T-cell adhesion and
200 infiltration. T-cell adhesion to the 3D endothelial tube did not increase with CXCL12 concentration,
201 although it did increase with time at all doses tested (Fig S3a). However, all doses of CXCL12
202 tested, regardless of tumor presence, led to significant differences in T-cell infiltration compared
203 to control chips, with the no-tumor version of the assay leading to greater overall T-cell infiltration
204 (Fig 2e,f). We especially noticed in no-tumor conditions an elevated baseline level of infiltration
205 even in the absence of chemokine, compared to the with-tumor assay (Fig 2e,f). One potential
206 disease-relevant explanation for this could be soluble inhibitory factors secreted by the tumor
207 cells. However, another explanation could be asymmetry of media consumption in the no-tumor
208 version of the assay (i.e. endothelial cells and T-cells only, and present in the top channel, with a
209 cell-free bottom channel), which may lead to a nutrient gradient that initiates nonspecific T-Cell
210 infiltration even in the absence of recombinant chemokine. What is more, ELISA-based diffusion
211 studies repeated with T-cells support that the no-tumor version of the assay is more permissive
212 to chemokine diffusion at all doses of chemokine tested (Fig S3b,c). Thus, more effective
213 chemokine diffusion may also explain why T-cell response saturates at lower doses in the no-
214 tumor assay (37.5 nM CXCL12) compared to the with-tumor version of the assay (150 nM
215 CXCL12) (Fig 2f).



216
217

218 **Figure 3: Migration and sprouting of 3D endothelium in response to rhCXCL12 in the LToC-**
 219 **Endo model.** (a), Hoechst and CD31 staining of the indicated conditions, for naive and activated
 220 T-cells, low and high T-cell seeding density, and CXCL11 and CXCL12 chemokines, on day 3.
 221 With no T-cells in the chips, (b) CD31 staining depicting 3D endothelium response to control,
 222 CXCL12, or CXCL11 conditions after 3 days in culture and (c) brightfield images showing
 223 endothelial response to CXCL12 or media control, with and without tumor cells, after 3 days in
 224 culture. In (a) through (c), middle channel width is 350 μ m as indicated by the vertical bars.
 225

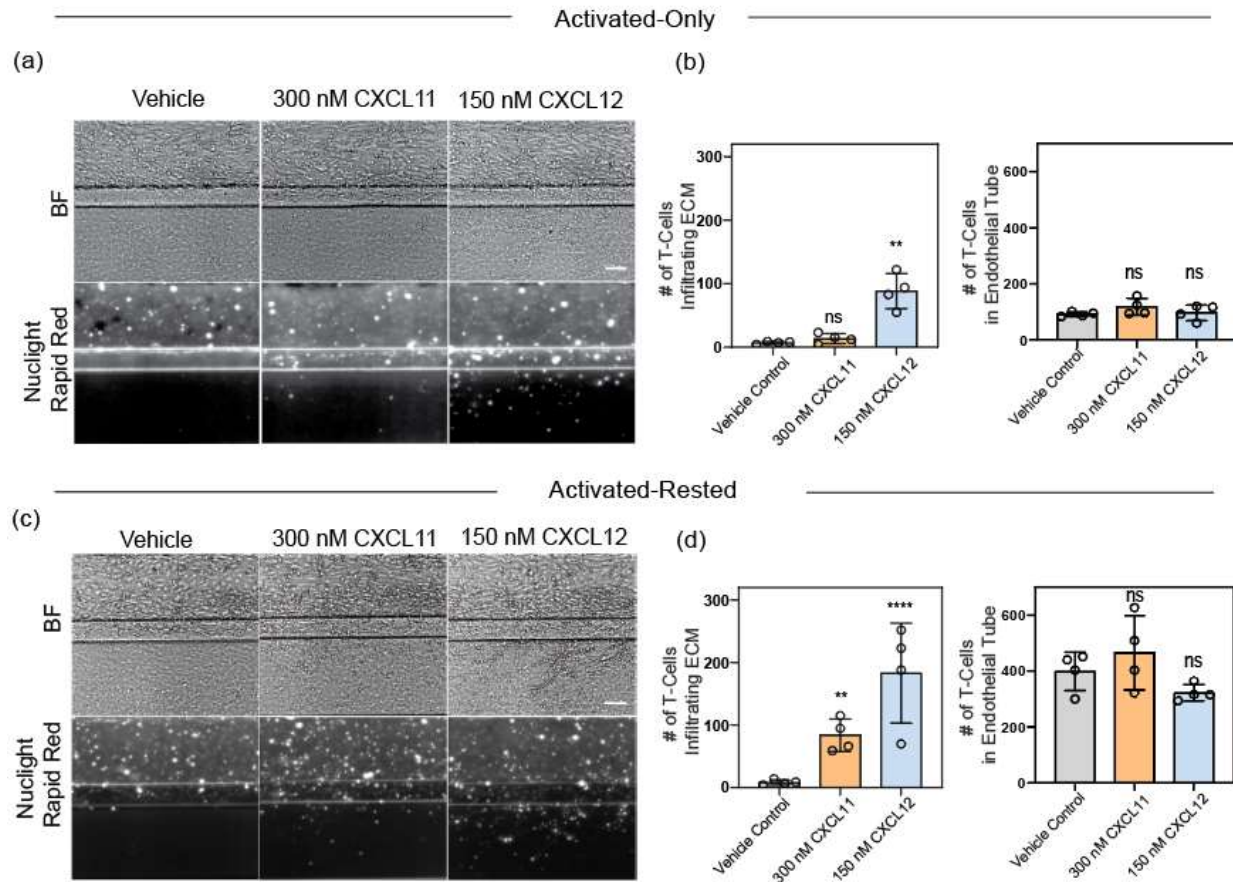
226 *Presence and activation of T-cells influence endothelial activation in response to CXCL12*

227

228 In the LToC-Endo, we observed notable differences in endothelial tube response to CXCL12
229 depending on the presence of activated T-cells. While CXCL12 drives migration or angiogenic
230 sprouting with naïve T-cells (Fig 3a) or when T-cells were absent (Fig 3b,c), we did not observe
231 pervasive endothelial cell activation when introducing activated T-cells (Fig 3a). CXCL12 is a
232 known driver of T-cell chemotaxis, but it is also a crucial regulator of angiogenesis. It acts by
233 increasing VEGF-A production in endothelial cells, which then upregulates their CXCR4
234 expression, enhances responsiveness to CXCL12, and contributes to an amplifying angiogenic
235 signaling loop[19]–[21]. CXCL12 also promotes angiogenesis through Akt activation via atypical
236 CXCR7 receptors, which are overexpressed only in stressed endothelial cells[22]. Under pro-
237 angiogenic signaling, the endothelium responds by increasing endothelial wall permeability,
238 destabilizing the vessel wall, and increasing expression of leukocyte adhesion receptors, in
239 addition to increasing endothelial cell proliferation and migration[21], [23]–[25]. It is possible that
240 these CXCL12-mediated endothelial events indirectly contribute to the observed window in T-cell
241 infiltration (Fig 2b-f), in addition to the direct effect of CXCL12 driving T-cell chemotaxis. By
242 contrast, CXCL11 is an angiostatic chemokine, known to counterbalance the vascular changes
243 described above[21]. Therefore, as expected we do not see angiogenic sprouting in response to
244 this chemokine in the assay. (Fig 3).

245

246 The reduction in migration and angiogenic sprouting responsiveness to CXCL12 suggests that
247 the 3D endothelium in the LToC-Endo may be under stress with the addition of activated T-cells.
248 Images of the 3D endothelium, 3 days after activated T-cell addition, show large holes that are
249 suggestive of endothelial stress (Fig 3a). Abundant T-cell proliferation is suspected to play a role,
250 as both in-chip and off-chip T-cells exhibit an expected, post-activation proliferative burst (Fig S4),
251 leading to a higher effective number of T-cells than initially seeded. As a consequence, the rapidly
252 proliferating T-cells may not only be contributing to endothelial stress at long time points, but also
253 diluting live cell dye, all of which may contribute to the plateau or decline in infiltrated T-cells after
254 2 days, which was seen both here (Fig 2c) and in a previous study [18].



255
256
257
258
259
260
261
262
263
264
265
266
267
268
269
270
271

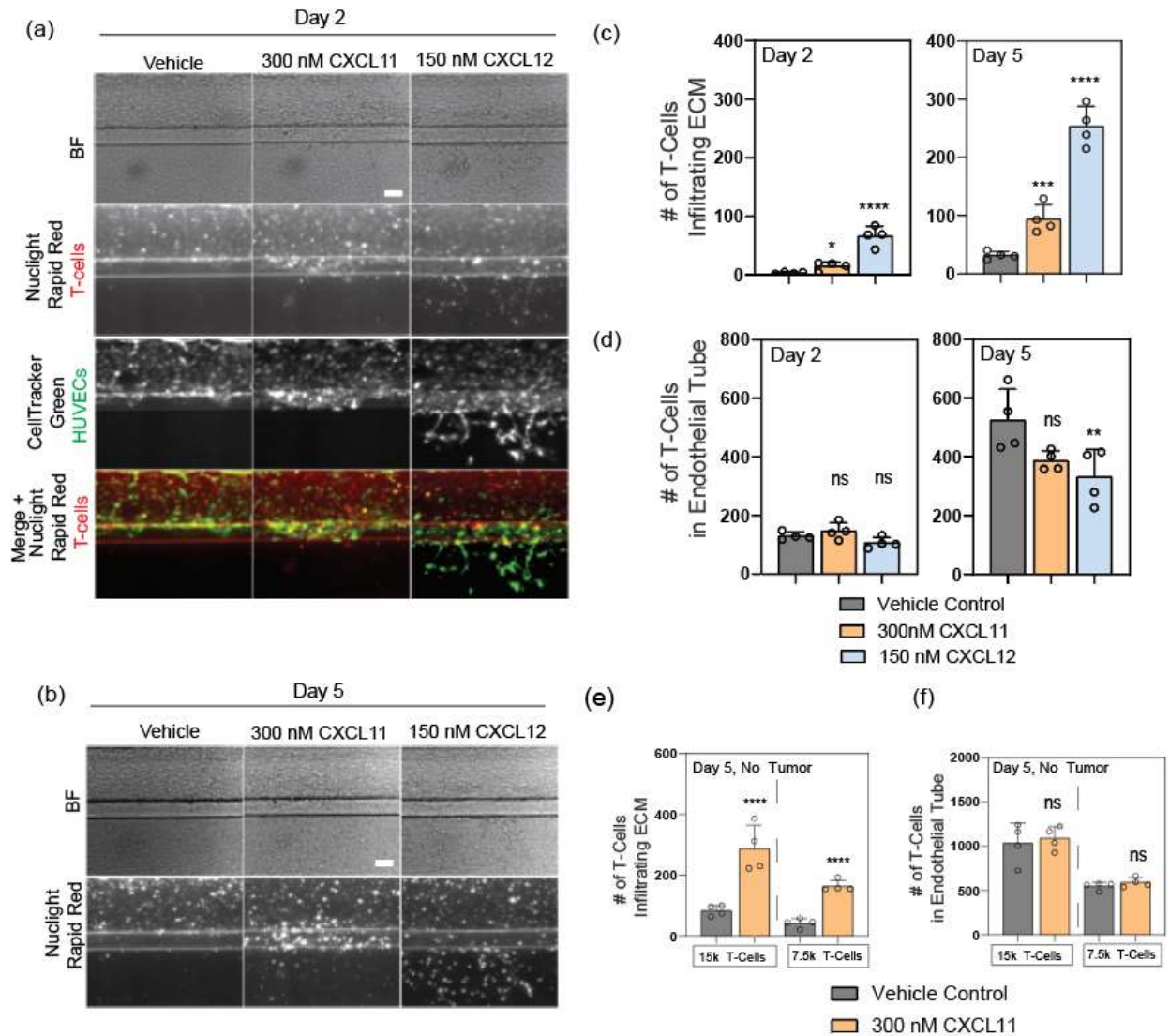
Figure 4: Activated-rested T-cell protocol enhances T-cell adhesion and chemotaxis, and restores CXCL12-driven endothelial activation, in the LToC-Endo. Representative brightfield and fluorescent images of T-cells (15k per chip) within the endothelial tubule and infiltration into the ECM compartment in response to the chemokine and dose indicated, at Day 2 time point, for (a) Activated-Only T-cells (AIMV) and (c) Activated-Rested T-cells (RPMI). Refer to supplement for flow cytometry controls that include additional Activated-Only (RPMI) condition. Scale bars in (a) and (c) are 100 μ m. In (b) and (d), quantifications of infiltrated T-cells and T-cells within the endothelial tube for both T-cell preparation protocols, respectively. Markers indicate mean T-cell numbers per chip ($n = 4$ per condition), bars indicate mean T-cell numbers per condition, and error bars indicate SD. Statistical testing was performed on square root transformed data to satisfy criteria of equal standard deviations. Significant differences between chemokines and respective vehicle alone controls are shown (One-way ANOVA corrected for multiple comparisons, * $p < 0.05$, *** $p < 0.0001$).

272 *Alternate T-cell activation protocol impacts T-cell phenotype and enhances functional response*

273 We hypothesized that the introduction of a rest period, mimicking the time lag between T-cell
274 activation and homing to a tumor site *in vivo*[6], would allow us to overcome the proliferative burst
275 prior to seeding activated T-cells. Additionally, we switched to a live nuclear dye which we
276 expected would be stable over longer culture periods. We performed the assay side-by-side with
277 activated or activated-rested T-cells. As expected, the activated-rested T-cells, which undergo
278 proliferative burst during the 2-day rest, increase in concentration by 3-4x prior to seeding,
279 compared to the activated-only T-cells (Fig S5a). Surprisingly, in spite of the lack of in-chip
280 proliferative burst, activated-rested T-cells adhered to the endothelium and infiltrated in greater
281 numbers in response to CXCL11 (~4x more on average) and CXCL12 (~2x more on average),
282 compared to activated-only T-cells (Fig 4a-d). To better understand these changes, we profiled
283 T-cells prepared using both approaches for expression of CXCR3 and CXCR4, the cognate
284 receptors for CXCL11 and CXCL12. We saw that the introduction of a rest period following a T-
285 cell activation enhanced CXCR3 and CXCR4 expression in all T-cell subsets compared to
286 activation-only T-cells, increasing the overall proportion of double positive (CXCR3+CXCR4+) T-
287 cells from ~30-50% to ~85% (Fig S5b, Table 1). Furthermore, we observed that the rest period
288 led to more central and effector memory T-cell phenotypes, indicating a more durably activated
289 state [26] (Fig S5c, Table 1). Our incorporation of an additional control in these studies allowed
290 us to attribute changes in T-cell phenotype to differences in activation regimen, rather than culture
291 medium, as this was also changed (Fig S5b,c; Table 1). Altogether, these data suggest that
292 implementing a T-cell culture protocol with activation followed by a rest period enables the
293 introduction of T-cells that are more sensitive and responsive into the tumor-on-chip assay.

294
295 With respect to endothelial tube responsiveness to CXCL12 chemokine, another key difference
296 emerged when switching from an activated-only to activated-rested T-cell culture protocol. With
297 the activated-only T-cells, a lack of response previously shown (Fig 3a) was reproduced (Fig 4a),
298 whereas in activated-rested T-cell chips, we observed endothelial migration in response to
299 CXCL12 by 48h (Fig 4c). This endothelial response to CXCL12 with activated-rested T-cells
300 appears to match more closely the endothelial response to CXCL12 with the naïve and no-T-cell
301 conditions (Fig 3). These data lead us to infer that adding rested T-cells minimizes the stress on
302 3D endothelial tubes caused by T-cell addition, and may preserve more physiologically relevant
303 responsiveness of the 3D endothelium to angiogenic cues.

304



305
306

307 **Figure 5: Activated-Rested T-cells enable an extended assay endpoint.** (a) and (b),
 308 Representative brightfield and fluorescent images of T-cell infiltration in response to the indicated
 309 chemokines and doses, on Days 2 and 5, for assay with 15k T-cells seeded and with tumor barrier.
 310 Scale bars are 100 μ m. (c), Quantifications of infiltrated T-cells and (d) T-cells within the
 311 endothelial tubes on Days 2 and 5, for the assay with tumor barrier. Day 5 quantifications from
 312 studies without tumor barriers, of (e) infiltrated T-cells and (f) T-cells within the endothelial tubes,
 313 for two different T-cell seeding densities. In (c) through (f), markers indicate T-cell numbers per
 314 chip ($n = 4$ per condition), bars indicate mean T-cell numbers per condition, and error bars indicate
 315 SD. In (c) and (e), statistical testing was performed on square root transformed data to satisfy
 316 criteria of equal standard deviations. Significant differences between chemokines and respective
 317 vehicle controls are shown (One-way ANOVA corrected for multiple comparisons, * $p < 0.05$, **
 318 $p < 0.01$, **** $p < 0.0001$).

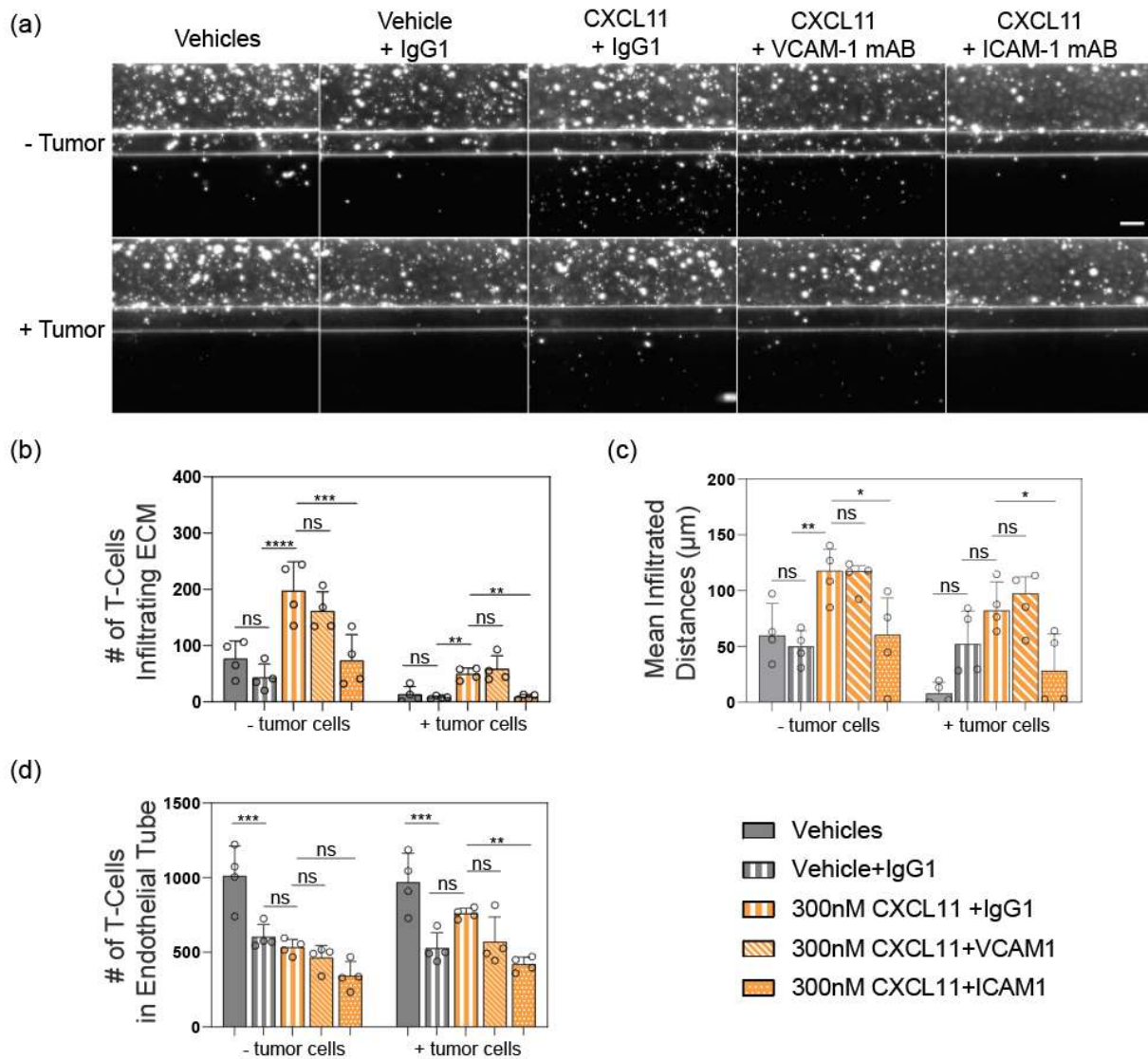
319

320 *Assay timeline extension is facilitated by alternate T-cell activation protocol*

321

322 Given that an activated-rested T-cell protocol allowed us to circumvent proliferative burst in-chip,
323 preserve 3D endothelium responsiveness to activation, and mitigate live cell dye dilution, we
324 hypothesized that we could extend the assay timeline. Repeating the assay with activated-rested
325 T-cells, we compared day 2 and day 5 time points. While the activated-only T-cell version of the
326 assay results in a decline in T-cell infiltration after day 2 (Fig 2c) and complete endothelial
327 dissolution by day 5, the activated-rested T-cell version of the assay shows higher levels of T-cell
328 adhesion and infiltration and more intact endothelium by day 5 (Fig 5a-d, Fig S6). While by day
329 2 we observe comparable levels of T-cell adhesion between control and chemokine conditions,
330 by day 5 we observe significantly fewer T-cells adherent in the CXCL12 condition. This may reflect
331 that although higher numbers of T-cells adhere to the endothelium over time in all conditions, a
332 significant number have migrated due to extravasation in the CXCL12 condition (Fig 5d).
333 Furthermore, we confirm that with this new T-cell activation strategy and extended timeline, T-cell
334 adhesion and infiltration still scales with T-cell seeding density, as observed in prior studies (Fig
335 5e,f). Finally, T-cell infiltration remains greater when the tumor barrier is absent than when the
336 tumor barrier is present, reflecting a trend previously observed (Fig 5c,e). Overall, these studies
337 support that the adoption of an activated-rested T-cell culture protocol and a long-lasting, live
338 nuclear dye enable assay timeline extension.

339



340

341

342 **Figure 6: T-cell extravasation and chemotaxis in response to CXCL11 are dependent on**

343 **ICAM-1 endothelial receptor in the tumor on chip platform.** (a) Representative fluorescent

344 images of T-cell infiltration in response to chemokine or vehicle control, with additional treatment

345 as indicated with blocking antibody or IgG control. Images show Day 5 assay data both without

346 and with tumor barrier. Scale bar is 100 μ m. Per-chip day 5 quantifications of (b) mean infiltrated

347 T-cell number, (c) median infiltrated distance, and (d) mean T-cell number within the endothelial

348 tubes for all conditions tested. In (b-d), markers indicate T-cell numbers per chip (n = 4 per

349 condition), bars indicate mean T-cell numbers, and error bars indicate SDs. Significant differences

350 between chemokines and respective vehicle alone controls, with or without antibody treatments,

351 are shown (One-way ANOVA corrected for multiple comparisons, *p < 0.05, ** p < 0.01, ***

352 p < 0.001, **** p < 0.0001). In (b), statistical testing was performed on square root transformed data

to satisfy criteria of equal standard deviations.

353 *T-cell chemotaxis in tumor on chip requires ICAM-1*

354

355 Finally, we evaluated the ability of this tumor on chip microphysiological system to recapitulate
356 mechanisms of T-extravasation. Tumor infiltration requires chemokine-induced polarization of T-
357 cells and attachment to the endothelium through VCAM-1/ICAM integrin activity[27], [28].
358 Therefore, we repeated this assay using CXCL11 as the chemotactic stimulus, and added
359 blocking antibodies against endothelial receptors VCAM-1 and ICAM-1 or isotype controls at the
360 same time as adding chemotactic triggers.

361

362 By Day 5 of T-cell incorporation into the platform, we observe that ICAM-1 blocking antibody
363 treatment significantly impacts the number of T-cells infiltrating into the extracellular matrix in
364 response to CXCL11, while VCAM-1 blocking antibody does not (Fig 6a,b). The median infiltration
365 distance of T-cells in chips with ICAM-1 blocking antibody is significantly reduced compared to
366 those with isotype control (Fig 6c). These trends hold in with-tumor and without-tumor versions of
367 the assay (Fig 6a-c). We do observe that the addition of IgG control antibody significantly impacts
368 the number of T-cells adhering to the endothelium, even in the absence of chemokine (Fig 6d).
369 In the presence of CXCL11, and in the with-tumor assay condition, we observe a significantly
370 lower number of T-cells adhering to the endothelium using ICAM-1 blocking antibody. Altogether,
371 these data suggest that blocking ICAM-1 is sufficient to reduce but not entirely block T-cell
372 adherence, extravasation, and chemotaxis. These findings are consistent with T-cells using
373 endothelial receptors other than ICAM-1 to adhere, extravasate, and infiltrate.

374

375 It is unclear why VCAM-1 blocking did not result in decreased adhesion and chemotaxis. In
376 preclinical animal models, VCAM-1 density and tumor perfusion are predictive of T-cell infiltration
377 and treatment response to adoptively transferred and endogenous T-cells[28]. However, blocking
378 VCAM-1 is only marginally effective at blocking T-cell adhesion to endothelial cells *in vivo*. By
379 contrast, combined blocking of CD49d/integrin- $\alpha 4$ (a VCAM-1 binding partner), and CD18/integrin
380 $\beta 2$ (an ICAM binding partner) offers substantially improved blocking, with this cocktail shown to
381 prevent T-cell mediated tumor rejection[28].

382

383 *In vitro*, the role of VCAM-1 and ICAM-1 in T-cell adhesion depends on both T-cell and endothelial
384 cell activation[29]. While ICAM-1 is the main ligand utilized by CD4+ T-cells to adhere to IL-1-
385 induced HUVECs, memory T-cells can leverage a variety of adhesion pathways to bind to
386 HUVECs, including VCAM-1, ICAM-1, ELAM-1, and other ICAM ligands[29]. Upon T-cell
387 phenotyping here, we noted a switch from activated-only to activated-rested T-cells leads to a
388 shift toward central and effector memory phenotypes (Fig. S5c). More memory T-cells, utilizing
389 a greater variety of adhesion pathways to achieve arrest on and extravasation through the
390 endothelium, perhaps explains the enhanced T-cell adhesion and chemotaxis observed switching
391 from the activated-only to activated-rested protocol (Fig 4b,d) as well as the partial blocking of T-
392 cell infiltration using ICAM-1 blocking antibody (Fig. 6).

393

394 **Conclusion and Future Outlook**

395

396 In conclusion, we developed a microfluidic lung tumor on chip assay with a 3D endothelium
397 (LToC-Endo) perfused with rocking flow to evaluate modulators of T-cell extravasation and
398 infiltration through 3D extracellular matrix in a non-small cell lung carcinoma (NSCLC) context.
399 Due to the orientation of the platform, T-cell chemotaxis takes place across the x-y plane. This
400 orientation readily facilitates snapshots of T-cell chemotaxis profiles across the stromal matrix,
401 making the assay amenable to phenotypic screening and migration time point analysis. In
402 alignment with a need for future work highlighted previously[18], we extended the assay timeline
403 and improved the assay window by introducing a rest period after T-cell activation and selecting

404 a long lasting, live nuclear dye. Similar to *in vivo*, activated T-cells in the LToC-Endo extravasate
405 and infiltrate in response to chemotactic gradients, and the living endothelial barrier responds to
406 pro-angiogenic cues through sprouting. We have also shown the dependence of T-cell infiltration
407 on the presence of non-small cell lung carcinoma cells and on ICAM-1 endothelial receptors.
408 While animal models typically recapitulate immune cold tumors, the LToC-Endo and described
409 chemotaxis assay can also recapitulate features of immune-excluded tumors (i.e. angiogenesis,
410 immune infiltration into stroma)[4]. Given differences in chemokines present and antigen-
411 presenting functions of endothelial cells between human and animal models[4], this assay will be
412 a valuable tool for probing humanized tumor-immune-endothelial multicellular interactions in
413 NSCLC and other cancers. Additionally, this *in vitro* assay simultaneously offers the ability to
414 observe compound efficacy (i.e. T-cell adhesion and infiltration) with safety (i.e. drug induced
415 vascular injury, exacerbated angiogenesis in the tumor microenvironment (TME)), bringing safety
416 information earlier into the discovery research pipeline.

417
418 Similar to what has been shown for an angiogenesis assay using this platform[30], the next step
419 will be to evaluate the reproducibility and robustness in the LToC-Endo. Establishing a positive
420 control with a clinically meaningful 2-5 fold window, yet without angiogenic side-effects, would be
421 ideal based on prognostic differences between immune phenotypes in colorectal cancer
422 tumors[31] and in alignment with robust assay design[32]. Further work is needed to validate the
423 translatability of the assay by using standard of care molecules and comparing outcomes to
424 clinical responses[33]. Moreover, there is a need to identify the T-cell subtypes that potential
425 therapeutics successfully induce to infiltrate; in this case, enhancement of CD8+ cytotoxic T-cells
426 is would be desirable. Future directions for the LToC-Endo involve incorporating the stromal cells
427 that perpetuate immune suppression in the TME, such as cancer-associated fibroblasts, myeloid
428 derived suppressor cells, and tumor-associated macrophages[34]–[36]. It will also be important
429 to evaluate how other immune cell types (i.e. T-regulatory cells, natural killer cells, and B-cells[3])
430 infiltrate into the TME in response to chemotactic cues and compounds, and to include a tumor
431 cell killing component into the assay. Altogether, we anticipate that the LToC-Endo complex in
432 vitro model will serve as a valuable tool to study multicellular and cell-extracellular matrix
433 mechanisms of immune suppression, screen for drug candidates that target these processes to
434 improve patient responses to immunotherapies.

435
436 For this complex in vitro model to support the refinement, reduction, and replacement of animal
437 immuno-oncology models, whether classical syngeneic (i.e. MC38, 4T1) or ‘humanized’ mouse
438 tumor models[37], a translational strategy is needed. We propose that noninvasive imaging
439 techniques serve as a translational link to align imaging-based pharmacodynamic (PD) timepoint
440 readouts between complex in vitro and in vivo models of immune infiltration. Noninvasive imaging
441 techniques can detect and monitor anatomical, functional, metabolic, or molecular-level changes
442 within the body of animals with minimal pain, distress, or premature termination[38], and can do
443 so in a temporal and spatial manner. For example, infiltration of specific T-cell populations (e.g.
444 CD8+) can be tracked into specific organs, tumors, or tumor-draining lymph nodes over time
445 within a single animal[39]. In this way, noninvasive imaging can enable comprehensive,
446 longitudinal immune response datasets to be derived from fewer animals, thereby increasing the
447 statistical power of the data gathered by reducing experimental variation[40]–[43]. This is in
448 contrast to traditional methods requiring animals to be sacrificed at given time points, i.e. using
449 histology and flow cytometry[37]. Instead of relying exclusively on these informative yet endpoint-
450 requirement techniques, which now include scRNAseq[41], they could instead be employed as-
451 needed to verify or supplement noninvasive longitudinal imaging. Ideally, these noninvasive *in*
452 *vivo* approaches would translate to evolving clinical imaging techniques, which are expected to
453 gather similar longitudinal immune infiltration data, monitor therapeutic response in individual
454 patients, and enable precision oncologic medicine[39]–[41].

455
456 With this translational strategy in mind, an imaging-based, humanized, immune infiltration
457 complex in vitro model such as the LToC-Endo would be well suited to establish an in vitro/in
458 vivo correlation. Longitudinal, imaging-based T-cell infiltration datasets, gathered per-chip, per-
459 animal, and per patient, could then be used to calibrate silico models, enable better in vivo
460 response prediction, refine the selection of candidates to progress into animal studies, and
461 ultimately provide better medicines to patients.

462
463 *Conflicts of Interest*

464 J.S. and L.v.d.B are employees of Mimetas BV. K.M.W., B.S., T.S.P.G., A.C., M.L., S.T., A.G.,
465 S.-H.C., D.P., N.S., S.G., and J.E. are employees of GSK, or were at the time of producing this
466 work. The OrganoPlate® is a registered trademark of Mimetas BV.

467
468 *Data Availability Statement*

469 The datasets generated during and analyzed during the current study are available from the
470 corresponding author upon reasonable request.

471
472 *Author Contributions*

473 K.M.W., B.S., J.E., A.C., E.K., D.P., N.S., J.S., and L.v.d.B. conceived of ideas and planned
474 experiments. K.M.W., J.S., and L.v.d.B. led and performed key experiments. J.S. and K.M.W.
475 analyzed experimental data. D.P. and N.S. prepared T-cells and performed T-cell receptor
476 expression and phenotyping studies in GSK experiments. B.S., T.S.P.G, A.C., S.G., E.K.,
477 D.P., and N.S. provided input and feedback on experimental studies. S.T. designed high content
478 imaging protocols and data acquisition workflows for GSK experiments. M.L. designed GSK
479 automated analysis pipeline for experimental data. A.G. provided recommendations for data
480 analysis and statistical testing. K.M.W. prepared and wrote the manuscript, and S.G., T.S.P.G.,
481 J.E., N.S., and S.-H.C. contributed to the final manuscript.

482
483 *Acknowledgements*

484 We gratefully acknowledge John Lowman for his facilitation of the collaborative research
485 agreement. Thank you to Kimberly Nadwodny and Ed Gimmi for their data integrity and patents
486 review, respectively. We also acknowledge Maggie Connelly for isolating T-cells for these
487 studies. Thank you to Jeremy Waight for providing helpful feedback on the presentation of this
488 work and the manuscript. This work was funded by GSK.

489 *Ethics Statement*

490 The human biological samples were sourced ethically, and their research use was in accord
491 with the terms of the informed consents under an IRB/EC approved protocol.

492

493 References

- 494
- 495 [1] C. Oelkrug and J. M. Ramage, "Enhancement of T cell recruitment and infiltration into
496 tumours," *Clin. Exp. Immunol.*, vol. 178, no. 1, pp. 1–8, 2014, doi: 10.1111/cei.12382.
- 497 [2] J. Zhang, S. Endres, and S. Kobold, "Enhancing tumor T cell infiltration to enable cancer
498 immunotherapy," *Immunotherapy*, vol. 11, no. 3, pp. 201–213, 2019, doi: 10.2217/imt-
499 2018-0111.
- 500 [3] L. L. van der Woude, M. A. J. Gorris, A. Halilovic, C. G. Figdor, and I. J. M. de Vries,
501 "Migrating into the Tumor: a Roadmap for T Cells," *Trends in Cancer*, vol. 3, no. 11, pp.
502 797–808, 2017, doi: 10.1016/j.trecan.2017.09.006.
- 503 [4] P. S. Hegde and D. S. Chen, "Top 10 Challenges in Cancer Immunotherapy," *Immunity*,
504 vol. 52, no. 1, pp. 17–35, 2020, doi: 10.1016/j.immuni.2019.12.011.
- 505 [5] T. Tokito *et al.*, "Predictive relevance of PD-L1 expression combined with CD8+ TIL
506 density in stage III non-small cell lung cancer patients receiving concurrent
507 chemoradiotherapy," *Eur. J. Cancer*, vol. 55, pp. 7–14, 2016, doi:
508 10.1016/j.ejca.2015.11.020.
- 509 [6] D. S. Chen and I. Mellman, "Oncology meets immunology: The cancer-immunity cycle,"
510 *Immunity*, vol. 39, no. 1, pp. 1–10, 2013, doi: 10.1016/j.immuni.2013.07.012.
- 511 [7] J. Mestas and C. C. W. Hughes, "Of Mice and Not Men: Differences between Mouse and
512 Human Immunology," *J. Immunol.*, vol. 172, no. 5, pp. 2731–2738, 2004, doi:
513 10.4049/jimmunol.172.5.2731.
- 514 [8] N. Levy, "The use of animal as models: Ethical considerations," *Int. J. Stroke*, vol. 7, no.
515 5, pp. 440–442, 2012, doi: 10.1111/j.1747-4949.2012.00772.x.
- 516 [9] C. G. Sip, N. Bhattacharjee, and A. Folch, "Microfluidic transwell inserts for generation of
517 tissue culture-friendly gradients in well plates," *Lab Chip*, vol. 14, no. 2, pp. 302–314,
518 2014, doi: 10.1039/c3lc51052b.
- 519 [10] S. Boyden, "The chemotactic effect of mixtures of antibody and antigen on
520 polymorphonuclear leucocytes," *J. Exp. Med.*, vol. 115, no. 3, pp. 453–466, 1962.
- 521 [11] C. Zhang, M. P. Barrios, R. M. Alani, M. Cabodi, and J. Y. Wong, "A microfluidic
522 Transwell to study chemotaxis," *Exp. Cell Res.*, vol. 342, no. 2, pp. 159–165, 2016, doi:
523 10.1016/j.yexcr.2016.03.010.
- 524 [12] K. M. Wisdom *et al.*, "Matrix mechanical plasticity regulates cancer cell migration through
525 confining microenvironments," *Nat. Commun.*, vol. 9, no. 1, 2018, doi: 10.1038/s41467-
526 018-06641-z.
- 527 [13] S. Herter *et al.*, "A novel three-dimensional heterotypic spheroid model for the
528 assessment of the activity of cancer immunotherapy agents," *Cancer Immunol.*
529 *Immunother.*, vol. 66, no. 1, pp. 129–140, Jan. 2017, doi: 10.1007/s00262-016-1927-1.
- 530 [14] J. Rodrigues, M. A. Heinrich, L. M. Teixeira, and J. Prakash, "3D In Vitro Model
531 (R)evolution: Unveiling Tumor–Stroma Interactions," *Trends in Cancer*, vol. xx, no. xx,
532 2020, doi: 10.1016/j.trecan.2020.10.009.
- 533 [15] T. H. Booij, L. S. Price, and E. H. J. Danen, "3D Cell-Based Assays for Drug Screens:
534 Challenges in Imaging, Image Analysis, and High-Content Analysis," *SLAS Discov.*, vol.
535 24, no. 6, pp. 615–627, 2019, doi: 10.1177/2472555219830087.
- 536 [16] H. Salmon *et al.*, "Matrix architecture defines the preferential localization and migration of
537 T cells into the stroma of human lung tumors," *J. Clin. Invest.*, vol. 122, no. 3, pp. 899–
538 910, Mar. 2012, doi: 10.1172/JCI45817.
- 539 [17] M. F. Krummel, F. Bartumeus, and A. Gérard, "T cell migration, search strategies and
540 mechanisms," *Nat. Rev. Immunol.*, vol. 16, no. 3, pp. 193–201, 2016, doi:
541 10.1038/nri.2015.16.
- 542 [18] L. de Haan *et al.*, "A microfluidic 3D endothelium-on-a-chip model to study
543 transendothelial migration of T cells in health and disease," *Int. J. Mol. Sci.*, vol. 22, no.

- 544 15, 2021, doi: 10.3390/ijms22158234.
- 545 [19] R. Salcedo *et al.*, “Vascular endothelial growth factor and basic fibroblast growth factor
546 induce expression of CXCR4 on human endothelial cells. In vivo neovascularization
547 induced by stromal-derived factor-1 α ,” *Am. J. Pathol.*, vol. 154, no. 4, pp. 1125–1135,
548 1999, doi: 10.1016/S0002-9440(10)65365-5.
- 549 [20] P. Staller, J. Sulitkova, J. Lisztwan, H. Moch, E. J. Oakeley, and W. Krek, “Chemokine
550 receptor CXCR4 downregulated by von Hippel-Lindau tumour suppressor pVHL,” *Nature*,
551 vol. 425, no. 6955, pp. 307–311, 2003, doi: 10.1038/nature01874.
- 552 [21] P. Romagnani, L. Lasagni, F. Annunziato, M. Serio, and S. Romagnani, “CXC
553 chemokines: The regulatory link between inflammation and angiogenesis,” *Trends*
554 *Immunol.*, vol. 25, no. 4, pp. 201–209, 2004, doi: 10.1016/j.it.2004.02.006.
- 555 [22] M. Zhang, L. Qiu, Y. Zhang, D. Xu, J. C. Zheng, and L. Jiang, “CXCL12 enhances
556 angiogenesis through CXCR7 activation in human umbilical vein endothelial cells,” *Sci.*
557 *Rep.*, vol. 7, no. 1, pp. 1–9, 2017, doi: 10.1038/s41598-017-08840-y.
- 558 [23] J. H. W. Distler, A. Hirth, M. Kurowaska-Stolarska, R. E. Gay, S. Gay, and O. Distler,
559 “Angiogenic and angiostatic factors in the molecular control of angiogenesis,” *Q. J. Nucl.*
560 *Med.*, vol. 47, no. 3, pp. 149–61, 2003.
- 561 [24] B. J. Hunt and K. M. Jurd, “Endothelial cell activation,” *Br. Med. J.*, vol. 316, no. 7141, pp.
562 1328–1329, 1998, doi: 10.1136/bmj.316.7141.1328.
- 563 [25] R. M. Strieter, M. D. Burdick, B. N. Gomperts, J. A. Belperio, and M. P. Keane, “CXC
564 chemokines in angiogenesis,” *Cytokine Growth Factor Rev.*, vol. 16, no. 6, pp. 593–609,
565 2005, doi: 10.1016/j.cytogfr.2005.04.007.
- 566 [26] Y. D. Mahnke, T. M. Brodie, F. Sallusto, M. Roederer, and E. Lugli, “The who’s who of T-
567 cell differentiation: Human memory T-cell subsets,” *Eur. J. Immunol.*, vol. 43, no. 11, pp.
568 2797–2809, 2013, doi: 10.1002/eji.201343751.
- 569 [27] R. J. Melder, L. L. Munn, S. Yamada, C. Ohkubo, and R. K. Jain, “Selectin- and integrin-
570 mediated T-lymphocyte rolling and arrest on TNF-alpha-activated endothelium:
571 augmentation by erythrocytes,” *Biophys. J.*, vol. 69, no. 5, pp. 2131–2138, 1995, doi:
572 10.1016/S0006-3495(95)80087-1.
- 573 [28] J. Riegler *et al.*, “VCAM-1 Density and Tumor Perfusion Predict T-cell Infiltration and
574 Treatment Response in Preclinical Models,” *Neoplasia (United States)*, vol. 21, no. 10,
575 pp. 1036–1050, 2019, doi: 10.1016/j.neo.2019.08.003.
- 576 [29] Y. Shimizu *et al.*, “Four molecular pathways of T cell adhesion to endothelial cells: Roles
577 of LFA-1, VCAM-1, and ELAM-1 and changes in pathway hierarchy under different
578 activation conditions,” *J. Cell Biol.*, vol. 113, no. 5, pp. 1203–1212, 1991, doi:
579 10.1083/jcb.113.5.1203.
- 580 [30] V. van Duinen *et al.*, “Robust and scalable angiogenesis assay of perfused 3D human
581 ipsc-derived endothelium for anti-angiogenic drug screening,” *Int. J. Mol. Sci.*, vol. 21, no.
582 13, pp. 1–9, 2020, doi: 10.3390/ijms21134804.
- 583 [31] F. Pagès *et al.*, “Effector Memory T Cells, Early Metastasis, and Survival in Colorectal
584 Cancer,” *N. Engl. J. Med.*, vol. 353, no. 25, pp. 2654–2666, 2005, doi:
585 10.1056/nejmoa051424.
- 586 [32] P. W. Iversen, B. J. Eastwood, G. S. Sittampalam, and K. L. Cox, “A comparison of assay
587 performance measures in screening assays: Signal window, Z’ factor, and assay
588 variability ratio,” *J. Biomol. Screen.*, vol. 11, no. 3, pp. 247–252, 2006, doi:
589 10.1177/1087057105285610.
- 590 [33] S. Baran, “Perspectives on the evaluation and adoption of complex in vitro models in drug
591 development: Workshop with the FDA and the pharmaceutical industry (IQ MPS
592 Affiliate),” *ALTEX*, vol. 39, no. 2, pp. 297–314, 2022, doi: 10.14573/altex.2112203.
- 593 [34] S. Mariathasan *et al.*, “TGF β attenuates tumour response to PD-L1 blockade by
594 contributing to exclusion of T cells,” *Nature*, vol. 554, no. 7693, pp. 544–548, Feb. 2018,

- 595 doi: 10.1038/nature25501.
- 596 [35] J. A. Joyce and D. T. Fearon, "T cell exclusion, immune privilege, and the tumor
597 microenvironment," *Science* (80-.), vol. 348, no. 6230, pp. 74–80, Apr. 2015, doi:
598 10.1126/science.aaa6204.
- 599 [36] R. M. Bremnes *et al.*, "The role of tumor stroma in cancer progression and prognosis:
600 Emphasis on carcinoma-associated fibroblasts and non-small cell lung cancer," *J.*
601 *Thorac. Oncol.*, vol. 6, no. 1, pp. 209–217, 2011, doi: 10.1097/JTO.0b013e3181f8a1bd.
- 602 [37] L. Zitvogel, J. M. Pitt, R. Daillère, M. J. Smyth, and G. Kroemer, "Mouse models in
603 oncoimmunology," *Nat. Rev. Cancer*, vol. 16, no. 12, pp. 759–773, 2016, doi:
604 10.1038/nrc.2016.91.
- 605 [38] B. Beckmann, N. and Ledermann, "Noninvasive Small Rodent Imaging: Significance for
606 the 3R Principles," in *Small Animal Imaging*, 2017.
- 607 [39] M. Rashidian *et al.*, "Predicting the response to CTLA-4 blockade by longitudinal
608 noninvasive monitoring of CD8 T cells," *J. Exp. Med.*, vol. 214, no. 8, pp. 2243–2255,
609 2017, doi: 10.1084/jem.20161950.
- 610 [40] R. Weissleder, M. C. Schwaiger, S. S. Gambhir, and H. Hricak, "Imaging approaches to
611 optimize molecular therapies," *Sci. Transl. Med.*, vol. 8, no. 355, pp. 1–8, 2016, doi:
612 10.1126/scitranslmed.aaf3936.
- 613 [41] M. Rashidian *et al.*, "Immuno-PET identifies the myeloid compartment as a key
614 contributor to the outcome of the antitumor response under PD-1 blockade," *Proc. Natl.*
615 *Acad. Sci. U. S. A.*, vol. 116, no. 34, pp. 16971–16980, 2019, doi:
616 10.1073/pnas.1905005116.
- 617 [42] F. Alsaid, H., Cheng, S.H., Bi, M., Rambo, M.V., Skedzielewski, T., Hoang, B., Mohanan,
618 S., Gehman, A., Hsu, C.Y., Doan, M. and Xie, "Immuno-PET monitoring of CD8+ T cell
619 infiltration post anti-ICOS agonist antibody treatment alone and in combination with PD-1
620 blocking antibody using a 89Zr anti-CD8+ mouse minibody in EMT 6 syngeneic tumor
621 mouseitile," in *Cancer Research*, 2021, p. 2816.
- 622 [43] R. Tavaré *et al.*, "Engineered antibody fragments for immuno-PET imaging of
623 endogenous CD8 + T cells in vivo," *Proc. Natl. Acad. Sci. U. S. A.*, vol. 111, no. 3, pp.
624 1108–1113, 2014, doi: 10.1073/pnas.1316922111.
- 625 [44] S. Van Der Walt *et al.*, "Scikit-image: Image processing in python," *PeerJ*, vol. 2014, no.
626 1, pp. 1–18, 2014, doi: 10.7717/peerj.453.
- 627 [45] N. Dey, "Uneven illumination correction of digital images: A survey of the state-of-the-art,"
628 *Optik (Stuttg.)*, vol. 183, no. February, pp. 483–495, 2019, doi:
629 10.1016/j.ijleo.2019.02.118.
- 630 [46] S. J. Trietsch *et al.*, "Membrane-free culture and real-time barrier integrity assessment of
631 perfused intestinal epithelium tubes," *Nat. Commun.*, vol. 8, no. 1, pp. 1–7, 2017, doi:
632 10.1038/s41467-017-00259-3.
- 633
- 634

635 **Materials and Methods**

636

637 *Cell Culture and Media*

638 All human biological samples were sourced ethically, and their research use was in accord with
639 the terms of the informed consents under an IRB/EC approved protocol. Human Umbilical Vein
640 Endothelial Cells (HUVECs) (Lonza, pooled donor) were cultured in complete human endothelial
641 medium (Cell Biologics), expanded, and bio-banked in aliquots. HUVECs in all studies were used
642 at or before passage 5. HCC0827 cells (University of Texas Southwestern) were cultured in RPMI
643 (Gibco) + 5% FBS (Gibco). Primary human T-Cells (Peripheral Blood, Cryopreserved, CD3+ Pan
644 T Cells, Negatively Selected CD 3+, AllCells) were thawed in one of the following media solutions,
645 as indicated in the studies described: either AIM V medium (Gibco) containing 20 IU/mL of IL-2
646 (Miltenyi) or RPMI + 10% FBS. For activated T-Cells, 1:500 TransAct (Miltenyi) was added to the
647 medium. Activated-only T-cells were cultured for 48 hours (either with or without 1:500 TransAct)
648 prior to use in assay. Activated-rested T-Cells were cultured for 72 hours in 1:500 TransAct,
649 followed by a 48-hour rest period, during which time the medium was washed out via
650 centrifugation and replaced with RPMI + 10% FBS.

651

652 *T-Cell Isolation*

653 T-cells were obtained directly from AllCells and shipped to the MIMETAS research facility, or they
654 were isolated from AllCells leukopaks internally at GSK. For this, T-cells were isolated from full
655 fresh leukopaks (AllCells). Leukopaks were received and stored at 4C overnight (approx. 16h).
656 First, Peripheral Blood Mononuclear cells (PBMCs) were isolated using a Custom PBMC Isolation
657 Kit (Miltenyi), using magnetic beads to isolate out erythrocytes and granulocytes on magnetically
658 charged cell selection columns while eluting PBMCs. T-cells were then isolated from the PBMCs
659 using a standard Pan T Isolation kit (Miltenyi) using manufacturer protocols. T-cells were
660 cryopreserved in CS10 (BioLife Solutions, 210102) in a rate-controlled freezer over the course of
661 one hour, and transferred to LN2 storage.

662

663 *T-Cell Chemotaxis and Infiltration Assay*

664 Mimetas 3-lane 400 um Organoplate® (MIMETAS) was used for these studies. To seed the plates
665 with collagen (Day -2, indexed to T-cell addition day), 50 uL of DPBS was added into the
666 observation port to facilitate making chip filling visible. To form the extracellular matrix barrier, Rat
667 tail collagen-1 (Cultrex) was mixed with HEPES and 37 g/L NaHCO₃ in a 8:1:1 ratio to form a 4
668 mg/mL collagen-1 solution. These components were mixed well > 20 times, being careful not to
669 generate bubbles. Within 10 minutes, 1.8 uL gel solution was seeded into each chip using an
670 automatic repeater pipette (Sartorius). The Organoplate® was then placed in a humidified
671 incubator (37°C, 5% CO₂) for 15 minutes to allow polymerization of the collagen-1 gel. 30 uL
672 PBS was then added into the gel inlet to hydrate the ECM layer prior to returning the plate to the
673 incubator. To form the 3D endothelium, HUVECs were trypsinized, resuspended in endothelial
674 medium, counted using an automated cell counter (ViCell Blu, Beckman Coulter), and
675 resuspended to a cell seeding density of 10e6 cells/mL. PBS was removed from the gel inlets,
676 and 2 uL of cell suspension was deposited into the top inlet port using the automatic repeater
677 pipette. Cell suspension was regularly mixed in order to ensure homogenous cell seeding density.
678 After, 50 uL of endothelial medium was added to the same top medium inlet in which the cells
679 were deposited. The Organoplate® was placed with the lid forming a 75 degree angle against
680 the plate stand, and left in this orientation for around 3 hours in order to allow cells to attach. After
681 cell attachment, 50 uL of endothelial medium was added into the top medium outlet. The plate
682 was then placed on the Organoflow®, set to an inclination of 7° and an interval of 8 minutes, in
683 a humidified incubator.

684

685 On Day -1, tumor cells or empty medium were seeded into the bottom channel using a different
686 seeding strategy. Tumor cells (HCC0827) were trypsinized, resuspended in endothelial medium,
687 counted, and resuspended to a cell seeding density of 10e6 cells/mL. 2 uL of cell suspension was
688 then deposited into the bottom inlet port using the automatic repeater pipette. Cell suspension
689 was regularly mixed in order to ensure homogenous cell seeding density. The Organoplate® was
690 placed with the lid forming a 75 degree angle against the plate stand, but here with the plate
691 rotated 180 degrees from the previous HUVEC seeding step (i.e. top of the plate on the bottom,
692 touching the incubator shelf), and left in this orientation for around 3 hours in order to allow cells
693 to attach. After, 50 uL of endothelial medium was added into the inlet of the bottom perfusion
694 channel, and placed back on the OrganoFlow® rocker.

695
696 On Day 0, T-cells or empty medium controls were seeded into the OrganoPlate®. T-cells were
697 harvested gently, centrifuged at 300 x g for 5 minutes, counted, and incubated in dye solution,
698 either 2.5 uM CellTracker Orange CMRA (ThermoFisher) or 1:1000 NuLight Rapid Red
699 (Sartorius), in AIM V medium. For Nuclight Rapid Red dyed cells, cells were dyed at a
700 concentration of 1e6 cells/mL, with no more than 3e6 cells per falcon tube. Conicals of cells in
701 dye solutions were wrapped in foil and placed in an incubator for 30 mins. Halfway through the
702 incubation period, the tubes were inverted several times to gently mix. T-cells were then
703 centrifuged and pelleted to wash out the stain, and resuspended in Complete Assay Medium
704 containing AIM V Medium, 20 IU/mL, 5 ng/mL VEGF and 5 ng/mL bFGF. Cells were then counted
705 and diluted to desired concentration in Complete Assay Medium in order to deliver the number of
706 T-cells per chip indicated in these studies in 50 uL of medium. At this stage, the top medium
707 inlets and outlets were aspirated. 50 uL of T-cell solution was added into the top medium inlet,
708 and 50 uL Complete Assay Medium was added into the top medium outlet. Then, the bottom
709 medium inlet and outlets were aspirated, and replaced with 50 uL medium each containing
710 specified chemokine trigger or control medium solutions. For studies corresponding to Fig 3-5, a
711 half-volume medium re-addition was implemented, in which 25 uL of additional Complete Assay
712 medium were added into the top channel inlet and outlet, and 25 uL of chemokine trigger solution
713 were added into the bottom channel inlet and outlet. For antibody blocking experiments, vehicle
714 alone (PBS), IgG₁ antibody control (30 ug/mL, R&D Systems, MAB002), ICAM-1/CD54 (10ug/mL,
715 R&D Systems, BBA3) blocking antibody, or VCAM-1/CD106 (30ug/mL, R&D Systems, BBA5)
716 blocking antibody was added into the top channel inlets and outlets at the same time as
717 chemotactic trigger addition into the bottom compartment (Day 0) and also with the half medium
718 refresh (Day 2).

719 720 *T-Cell Imaging and Quantification*

721 For data obtained in Figures 1-2 and Supplementary Figures 1-6, images were acquired using a
722 spinning disc confocal and infiltrating T-cells were quantified using a custom FIJI macro as
723 previously described[18].

724
725 For data obtained in Figures 3-5 and Supplementary Figures 7-8, imaging was performed either
726 on EVOS microscope or a GE InCell 6500 high content confocal imaging system. Confocal z-
727 stacks acquired were converted into maximum intensity projection images, which were used for
728 analysis. Analyses were performed manually using ImageJ or using a custom python script. For
729 analysing migration distance of T-cells and the number that successfully infiltrate, a python script
730 was developed which utilised the open-source scikit-image library[44]. This analysis pipeline was
731 run in two stages: to accurately identify the PhaseGuides™ from the brightfield image, and
732 therefore the channel boundaries, and also to identify nuclei that had been stained with DAPI. In
733 order to identify PhaseGuides™, a synthetic image that mapped out the position of the
734 PhaseGuides™ was used as a template to convolve along the image in order to find the position

735 that looked most similar to the distribution of PhaseGuidesTM. To increase the accuracy of this
736 approach, the synthetic image was a 1pixel-width image with intensity bands that are similar to a
737 vertical cross-section of the PhaseGuidesTM (as it is 1 pixel wide, this is less affected by rotation).
738 Fast Normalized Cross Correlation was used for template matching and this led to a processed
739 image with ideally a single horizontal line that had been rotated as per the rotation of the plate.
740 Finding the maximum intensity (and therefore the highest correlation) along the x-axis enabled
741 binarizing the image and then edge detection was used. The original positions of PhaseGuidesTM
742 were then mapped back to this line. Separately, blob detection was used and the distances from
743 the blobs was measured using a signed distance function (i.e. distances are negative if they are
744 behind the line, and positive if they are in front). This meant that channels could be identified just
745 by the sign of the distances. Once the channels had been assigned to each nuclei, it was also
746 possible then to count the number of nuclei in chamber. To assist in detecting the
747 PhaseGuidesTM illumination correction was performed retrospectively by estimating the
748 illumination profile using a low-pass filter (using a Gaussian kernel with a large sigma)[45].
749

750 *Barrier Integrity Assays*

751 The barrier integrity of HUVEC endothelial tubes was evaluated before and after the addition of
752 T-cell compatible assay media as previously described[46], and the procedure is detailed within
753 the supplement of this publication[18]. Here, the top chip inlets and outlets were perfused with
754 0.5 mg/mL 20 kDa FITC Dextran (Sigma, FD20S).
755

756 *T-Cell Culture*

757 For activated-only T-cells, CD3+ T-cells were thawed, resuspended in assay medium (RPMI with
758 10% FBS and 20 IU/mL IL-2), and centrifuged (300xg, 5 mins) (ThermoFisher Scientific;
759 SORVALL ST16, SORVALL LEGEND, or XTR). Cell pellet was resuspended in assay medium
760 and counted using an automated cell counter (Vi-Cell XR, Beckman Coulter). Cells were then
761 diluted to a concentration of 1×10^6 cells/mL in assay medium and then activated using 1:500
762 TransAct. Cells were then added into a T25 flask and incubated at 37C, 5% CO₂ for 72 hours.
763 For activated-rested T-cells, the same procedure was followed as above, except cells were
764 cultured in TransAct for 48 hours. At this time, cells were harvested from flasks, spun down
765 (300xg, 5 mins) and resuspended in assay medium without TransAct. Cells were cultured for an
766 additional 48h rest period.
767

768 *Flow Cytometry*

769 Cells were plated at 300,000 cells/well in 96-well U-bottom plates (Corning). Plates were spun
770 down (300xg, 5 mins), washed 1x with 200 uL DPBS (Life Technologies), and spun down again
771 (300xg, 5 mins) to remove supernatant. For live/dead staining, live/dead dye was resuspended
772 as per manufacturer protocol and diluted in PBS at 1:100 dilution. 50 uL of diluted live/dead
773 solution was added to plate wells, mixed thoroughly, and incubated at room temperature for 15
774 minutes in the dark. Samples were washed 1X with 150 uL PBS and spun down (300xg, 5 mins)
775 to remove supernatant. For Fc blocking and primary antibody staining, 10 uL of Fc block (Miltenyi)
776 were added to each well and incubated for 10 mins in the dark at room temp. Then, 90 uL of
777 antibody cocktail (see details in antibodies and reagents section), prepared in FACs Buffer
778 (Beckton Dickenson) were added to each well and mixed. Samples were incubated for 30 mins
779 at 4C, wrapped in foil to protect from light. Wells were then washed 1X with 100 uL FACS Buffer
780 and 1X with 200 uL FACS Buffer. Plate was then spun down (300xg, 5 mins) and supernatant
781 removed. For sample fixation, 100 uL CytoFix fixation buffer (Beckton Dickenson) was added to
782 the wells and incubated at 25 mins at room temperature, wrapped in foil to protect from light.
783 Samples were then washed 1X with 100 uL FACS Buffer and 1X with 200 uL FACS Buffer, spun
784 down (300xg, 5 mins) and supernatant removed. Samples were resuspended in 250 uL FACS
785 Buffer and mixed well. Plates were stored at 4C until being read on the cytometer. Staining for

786 compensation controls was conducted on the day of flow analysis as follows. One drop of
787 UltraComp eBeads (eBiosciences) were incubated with 2 uL of the appropriate antibody for 30
788 mins at room temperature protected from light. For Aqua LIFE/DEAD dye compensation control,
789 2 drops ArC beads (Life Technologies) were incubated with 2 uL of Live/Dead dye for 30 mins, at
790 room temperature, protected from light. After incubation, beads were washed with flow buffer
791 (500 uL), centrifuged (300xg, 5 mins) and resuspended in 400uL of fresh flow buffer. One drop
792 of ArC negative beads were added to the Aqua tube, and then compensation was run. Flow
793 cytometry was conducted on the LSR Fortessa X-20 (Becton Dickinson), and data was analyzed
794 using FlowJo 10.6.2.

795

796 *Immunocytochemistry*

797 Cell cultures in the MIMETAS OrganoPlate® were fixed in 3.7% formaldehyde (Sigma) after 48h,
798 72h, or 120h in culture and immunostained as previously described[18]. Hoechst 33342 (Thermo
799 Fischer Scientific) was used to stain nuclei. Primary and secondary antibodies were used to stain
800 fixed cultures using products detailed in the antibodies and reagents section.

801

802 *Statistical Analysis*

803 Statistical analyses were performed using GraphPad Prism version 8.1.2 (332) for Windows,
804 GraphPad Software, San Diego, California USA, www.graphpad.com. Data were tested for
805 homogeneity in standard deviations, and were square root transformed if needed. Statistically
806 significant differences between means of two or more groups were evaluated using one-way
807 ANOVA (equal variance) or Brown-Forsythe and Welch ANOVA (Gaussian, unequal variance),
808 with multiple comparisons corrected using Dunnett's, Tukey's, or Sidak's. Differences were
809 considered significant if $p < 0.05$. s